crystals

MDPI

Article

A New Modification of $Rb[Al(NH_2)_4]$ and Condensation in Solid State

Christian Bäucker and Rainer Niewa *

Institute for Inorganic Chemistry, University of Stuttgart, Pfaffenwaldring 55, 70569 Stuttgart, Germany; baeucker@iac.uni-stuttgart.de

* Correspondence: rainer.niewa@iac.uni-stuttgart.de

Received: 19 October 2020; Accepted: 5 November 2020; Published: 9 November 2020

Abstract: A new modification of $Rb[Al(NH_2)_4]$ in space group *C*2/*c*, which differs from the known structural modification in the way the $[Al(NH_2)_4]^-$-tetrahedra are arranged in the surrounding area of the rubidium cation, was obtained from ammonothermal synthesis at 673 K and 680 bar. The crystal structure was determined by Rietveld refinements and further investigated by infrared and Raman spectroscopy. Thermal gravimetric investigations indicate two decomposition steps up to 450 °C, which can be assigned to ammonia leaving the material while the sample liquefies. During the third and final step, volatile rubidium amide is released, leaving nano-scaled cubic AlN behind. Investigating differently aged samples implies decomposition and condensation of amidoaluminate ions already at ambient temperature, which is supported by refinements of single crystal X-ray diffraction data, revealing lower nitrogen amounts than expected. The observed single crystal also exhibits a significantly smaller volume than the reported structures, further supporting the decomposition–condensation mechanism.

Keywords: ammonothermal synthesis; amide; aluminum

1. Introduction

Within the last decade, the continuing rise in the importance of semiconductors—for example, for LED technology—has also driven the need for new and improved semiconducting materials such as AlN [1], GaN [2], InN [3], InAs [4] or ZnO [5]. Mostly nitrides, the synthesis route for these materials often involves chemical vapor deposition (CVD) [6,7]. With CVD being a highly energy-consuming and elaborate method, ammonothermal synthesis—using supercritical ammonia as reaction medium (critical data T_c = 134.5 °C and p_c = 119 bar)—combines the scalability and production of freestanding superior high-quality nitride single crystals. The ammonothermal method derived from hydrothermal synthesis, the more commonly known solvothermal technique, was first utilized by Jacobs and Juza in 1966 [8]. It gained popularity as a superior method to obtain nitride crystals with high purity and low defect concentration. Although various groups have investigated the chemical properties of supercritical ammonia in synthesis over the years, there are still questions about the exact mechanisms during crystal growth in ammonothermal synthesis [9]. To determine and identify the existing species in supercritical state, so-called intermediates, which are typically solid products providing insight into the dissolved species, are synthesized at different temperatures and pressures and with the use of various mineralizers. Mineralizers are typically ammonoacids or -bases and serve to increase solubility. So far, in ammonothermal synthesis, mostly amidometalates have been found as intermediates when using ammonobasic mineralizers such as ANH_2 (A = Li − Cs) [9–11], while ammoniates are found when adding an ammonoacidic mineralizer like an ammonium halide (i.e., NH_4Cl) to the reaction [12].

The mineralizers not only increase solubility but also determine the dissolution and crystallization zone in the autoclave, depending on the temperature dependence of the solubility. Having a temperature

gradient when heated in a vertical furnace, ammonobasic mineralizers tend to result in crystallization in the zone of higher temperature; this means that, frequently, there is a retrograde solubility for ammonobasic systems [13,14]. For the ammonoacidic systems, both normal and retrograde solubility have been observed, being dependent on the administered temperature and used mineralizer [15,16].

While we have presented various solid intermediates in ammonoacidic [12] and particularly ammonobasic GaN crystal growth in recent years [17], we particularly obtained liquid phases upon using the amides of the heavier alkali metals K, Rb, and Cs [11]. The obtained ionic liquids can be characterized as losing ammonia even at ambient temperature, leading to partial condensation of amidogallate ions to form binuclear mixed amidoimidogallate ions. On the other hand, solid amidometalates appear to be prone to the formation of multiple modifications, as presented for various metals like aluminum, gallium or manganese in combination with alkali and alkaline earth metals [17–19]. The tetraamidoaluminate $Rb[Al(NH_2)_4]$ was earlier found to crystallize in the tetragonal space group *P*4/*n*; however, the presence of a second monoclinic modification in *P*2/*c* was already indicated but not structurally characterized [18]. Here, we report a modification of $Rb[Al(NH_2)_4]$ in *C*2/*c* and discuss data which indicate condensation of the amidoaluminate complex ions in solid state, as earlier observed in a similar manner in liquid for the corresponding Ga-containing system [11].

2. Materials and Methods

2.1. General Information

Since both the product and the starting materials are sensitive to air and moisture, all handling was done in a glove box filled with argon (MBraun, Garching, Germany, $p(O_2) < 0.1$ ppm). Synthesis experiments were conducted in custom-made autoclaves (98 mL volume, nickel-based alloy 718) [20]. For reaction purposes, one-side closed tubular furnaces were used (HTM Reetz GmbH, Berlin, Germany); this set-up causes a natural temperature gradient in the autoclave of around 100 K between the bottom and top of the reaction vessel, referred to as hot and cold zone. Any given temperature refers to what the furnace was brought up to, not the temperature inside the autoclave, which is lower depending on the temperature administered [21]. The maximum pressure inside the autoclave during the synthesis was observed by a digital pressure transmitter (P2VA1/5000 and DA2510, HBM GmbH Ismaning, Germany). After loading the autoclave with the starting materials, it was assembled, evacuated and flushed with ammonia once before using a dry-ice/ethanol cooling bath to condense the ammonia into the reaction vessel at approximately −72 °C. The NH_3 (99.999% anhydrous, Linde) was purified from H_2O, CO_2 and O_2 to a grade less than one ppbV with the use of a MicroTorr MC400-720F gas purifier (Rainer Lammertz pure gas products, Hürth, Germany). To correctly determine the amount of ammonia condensed into the autoclave, a self-built tensi-eudiometer after Hüttig was used [22]. The following chemicals were purchased and used as received: aluminum powder (99.97 metal basis, Alpha Aesar, Landau, Germany), $RbNH_2$ was synthesized by reaction of Rb in NH_3 at 383 K and 50 bar in 200 mL steel autoclaves (Carl Roth GmbH + Co. KG, Karlsruhe, Germany). The product was confirmed to be single-phase $RbNH_2$ by powder X-ray diffraction.

2.2. Synthesis

The new modification of $Rb[Al(NH_2)_4]$ was synthesized from the starting products with the following procedure: the autoclave was loaded with Al (204.04 mg, 7.413 mmol) and $RbNH_2$ (828.32 mg, 8.154 mmol), filled with ammonia (1.6886 mol) to a total of 43% and then heated to 673 K with a heating rate of 1.58 K min^{-1}, reaching a maximum pressure of 680 bar. The autoclave was kept at this temperature for a duration of 48 h and then cooled down to room temperature with a rate of 0.063 K min^{-1}. The product was collected in the form of colorless quadratic crystals next to microcrystalline powder from the hot zone of the autoclave. Powder diffraction of the product showed no traces of residue $RbNH_2$.

2.3. Characterization

X-ray diffraction on the microcrystalline powder (PXRD) was performed on a STADI-P (Stoe & Cie GmbH, Darmstadt, Germany) equipped with a position sensitive detector and copper K_α-radiation (λ = 1.5406 Å). The data were processed with the program WinXPow™ (version 3.0.1.13, Stoe & Cie GmbH, Darmstadt, Germany) and Rietveld refinements were carried out using the FULLPROF 2.05 program [23]. A visualization of the resulting structures was done with the program Diamond 4.0 (Crystal Impact GbR, Bonn, Germany).

Single crystal X-ray diffraction (scXRD) intensity data were measured on a Bruker–Nonius–Kappa CCD diffractometer with Molybdenum radiation (λ = 0.71073 Å). The structure was solved and refined using the program SHELX-97 [24]. CSD 2036338-2036339 contain the supplementary crystallographic data for this paper. These data can be obtained free of charge via http://www.ccdc.cam.ac.uk/conts/retrieving.html.

Investigations of thermal behavior were conducted on a STA 449 C (NETZSCH GmbH, Selb, Germany) fitted with an SiC furnace in corundum crucibles under continuous argon flow (Argon 5.0, Air Liquide, Düsseldorf, Germany). Measurement data were analyzed with the corresponding Proteus program package. The reaction chamber was evacuated and flushed with argon three times prior to any measurement.

Raman spectroscopy was performed on the microcrystalline powder sample as well as the single crystal with the help of an XploRA spectrometer (Horiba Jobin Yvon, Bensheim, Germany) and analyzed with the related software, LabSpec (V. 5.93.20). Infrared spectroscopy was carried out on a Nicolet iS5 (Thermo Fischer Scientific, Waltham, MA, USA).

3. Results and Discussion

When heating aluminum metal and $RbNH_2$ in an autoclave in supercritical ammonia to a furnace temperature of 673 K with a maximum pressure of 680 bar, a colorless substance is obtained from the hot area at the bottom of the autoclave. A typical temperature gradient within the autoclave is around 100 K for our autoclave setup [20]. The location of product formation indicates the retrograde temperature dependence of the solubility of the product, as is frequently observed for alkali metal amidometalates [13,14]. Powder X-ray diffraction results in a monoclinic unit cell with very similar unit cell parameters, as reported for a modification of $Rb[Al(NH_2)_4]$ of unknown crystal structure [18], however, with *C*-centering rather than primitive Bravais lattice (see Table 1). Interestingly, single crystals with the same unit cell relations and space group assignment but significantly smaller volume were obtained from the samples. A full structure refinement based on single crystal X-ray diffraction intensity data was prohibitive at first due to twinning and disorder phenomena; nevertheless, this led us to the initial structure model of $Rb[Al(NH_2)_4]$ in *C*2/*c* for Rietveld refinements of the powder X-ray diffraction data.

According to Rietveld refinements, the new monoclinic modification of $Rb[Al(NH_2)_4]$ crystallizes in the space group *C*2/*c* with a = 1048.48(7) pm, b = 539.39(3) pm, c = 1046.56(7) pm and β = 90.342(2)°. Additional information on crystal structure determination is given in Table 1; fractional position and displacement parameters are gathered in Table 2. Figure 1 shows a graphical representation of the refinement. A comparison of the experimental powder pattern with the simulated patterns for the crystal structure in *C*2/*c* and the known modification in *P*4/*n* already indicates strong similarities, which can be traced back to very similar arrangements of Rb and Al atoms in both structures, but also reveals additional prominent reflections (Figure 2).

It is obvious that the monoclinic structure emerges from the tetragonal modification as the diagonal between a_{tet} and b_{tet} becomes the new a_{mon} and c_{mon} axes, with the corresponding transformation matrix:

$$\boldsymbol{T} = \begin{pmatrix} 1 & 0 & 1 \\ 1 & 0 & \overline{1} \\ 0 & \overline{1} & 0 \end{pmatrix} \quad (1)$$

Table 1. Comparison of crystal structure data from PXRD and scXRD for the new monoclinic modification and results from literature [18]. For more information on the relation between structures obtained from powder and single crystal diffraction, compare main text body.

	PXRD	**scXRD**	**Jacobs et al. [18]**	
Crystal system	monoclinic	monoclinic	monoclinic	tetragonal
Space group	*C*2/*c*	*C*2/*c*	*P*2/*c*	*P*4/*n*
a (pm)	1047.68(9)	1040.21(6)	1051.9(3)	740.6(4)
b (pm)	538.99(4)	528.15(3)	541.9(4)	740.6(4)
c (pm)	1045.69(9)	1038.88(6)	1051.0(3)	538.6(4)
β °	90.338(3)	90.098(4)	90.30(2)	90
Z	4	4	4	2
Density (calc.) (g/cm^3)	1.986	2.055		
V (10^6 pm^3)	591.86(7)	570.75(6)	599.09	295.38
χ^2	1.56			
Radiation	Cu-$K\alpha_1$	Mo-$K\alpha$		
μ (mm^{-1})	12.00	8.7		
Monochromator	Germanium	Graphite		
Reflections collected/independent	85	10,833/664		
Parameters	16	49		
Temperature (K)	293	293		
Index ranges *h*/*k*/*l*		±13/±6/±13		
Pattern refined within	15.0–70.0°			
2-Theta max. (deg.)	70.00	54.90		
F(000)		344		
$R_1\|Fo\| \geq 4\sigma(Fo)$		0.0515		
$R_1/wR_2/GooF$		0.0579/0.1510/1.163		
Largest e- difference peak/hole (10^6 pm^{-3})		1.90/−0.64		
Twin matrix		$\begin{pmatrix} 0 & 0 & 1 \\ 0 & -1 & 0 \\ 1 & 0 & 0 \end{pmatrix}$		

Table 2. Fractional position and displacement parameters for the monoclinic modification of $Rb[Al(NH_2)_4]$ in space group *C*2/*c*, top: including atomic displacement parameters *B* (in 10^4 pm^3) from Rietveld refinements, bottom: with U_{eq} (in 10^4 pm^3) as calculated from single crystal data refinements.

Atom	**Wyckoff**	***x***	***y***	***z***	***B*/*U*$_{eq}$**	**Occ.**
Rb	4*c*	1/4	1/4	0	2.519	1
Al(1)	4*e*	0	0.4543 (23)	1/4	1.540	1
N(1)	8*f*	0.0299 (12)	0.2582 (32)	0.3786 (19)	3.079	1
N(2)	8*f*	0.3634 (17)	0.1792 (31)	0.2818 (14)	3.079	1
Rb	4*c*	1/4	1/4	0	0.0317 (3)	1
Al(1)	4*e*	0	0.4901 (6)	1/4	0.0201 (6)	0.834 (4)
Al(2)	4*e*	1/4	0.4670 (25)	1/4	0.0201 (6)	0.166 (4)
N(1)	8*f*	0.0274 (7)	0.2529 (10)	0.3847 (6)	0.0406 (26)	0.95 (4)
N(2)	8*f*	0.3651 (5)	0.2179 (10)	0.2758 (7)	0.0277 (22)	0.89 (3)

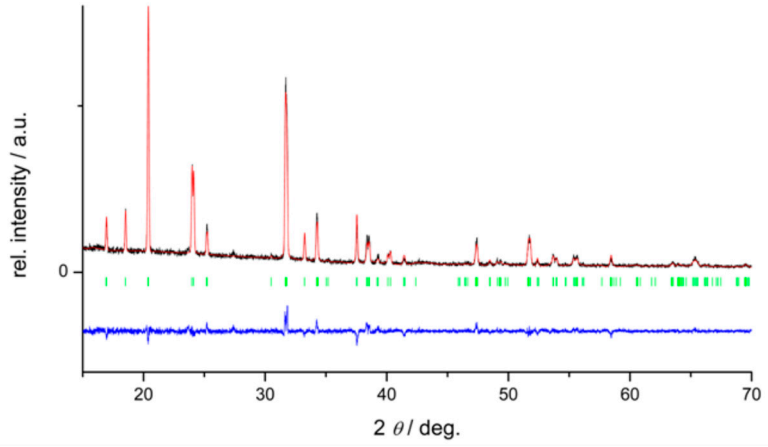

Figure 1. Rietveld refinement of the new modification of $Rb[Al(NH_2)_4]$ from PXRD data. Measured pattern in black, calculated pattern in red, possible Bragg reflections in green and difference curve in blue.

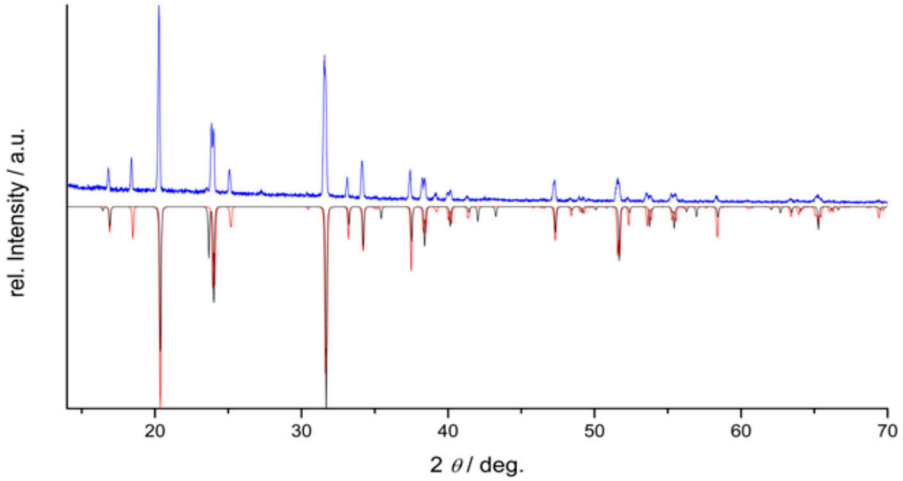

Figure 2. Comparison of experimental (blue) and simulated XRD patterns for $Rb[Al(NH_2)_4]$ in *C*2/*c* (red, new modification) and *P*4/*n* (black, known form). Note the presence of reflections at 18° and 25° as most prominent differences, well reproduced by the monoclinic structure model.

The main structural features of both modifications, the reported tetragonal and the new monoclinic form, are very similar: both contain tetrahedral tetraamidoaluminate ions, $[Al(NH_2)_4]^-$, as well as a cuboctahedral coordination of Rb^+. The distances between the aluminum and nitrogen atoms, however, differ slightly when compared, as a list of selected distances and angles (shown in Table 3) supports. We observe distorted tetrahedral coordination of Al in the monoclinic structure, while the tetragonal form shows four identical distances to N of the coordinating amido-ligands. When comparing the coordination environments of Rb, the distances are rather similar. In both, the cuboctahedral coordination is distorted, with four significantly shorter and eight longer distances, with the monoclinic modification exhibiting more strongly distorted cuboctahedra, however, with a nearly identical average distance. In both structures, these cuboctahedra are connected by face-sharing of opposite square faces forming strands, along the *c*-axis for the tetragonal modification and along the *b*-axis for the monoclinic one (compare Figure 3). Cuboctahedra of neighboring strands share edges, leading to the same motif for both modifications, only with tilting of the cuboctahedra of neighboring strands relative to each other in the monoclinic form (Figure 4).

Table 3. Distances and angles as calculated from the Rietveld refinement and single crystal data of $Rb[Al(NH_2)_4]$ in space group *C*2/*c*. The distances and angles of the known tetragonal modification have been added to the table for comparison.

Distances	This Work, PXRD	This Work, scXRD	Jacobs et al. [18]
Rb–N	2 × 319.3 (14)	2 × 310.8 (7)	4 × 316.7 (17)
	2 × 320.4 (14)	2 × 312.6 (7)	4 × 376.3 (22)
	2 × 346.3 (15)	2 × 360.2 (6)	4 × 377.4 (22)
	2 × 373.1 (15)	2 × 369.8 (1)	
	2 × 379.3 (15)	2 × 372.0 (1)	
	2 × 401.5 (16)	2 × 384.3 (2)	
Al(1)–N	2 × 173.7 (20)	2 × 187.0 (6)	4 × 182.5 (21)
	2 × 190.7 (19)	2 × 189.8 (6)	
Al(2)–N		2 × 194.3 (11)	
		2 × 207.8 (11)	
Al(1)–Al(2)		251.9 (14)	
Angles	**This Work, PXRD**	**This Work, scXRD**	**Jacobs et al. [18]**
N(1)–Al(1)–N(1)	101.0 (15)°	97.471 (1)°	2 × 103.9 (1)°
N(2)–Al(1)–N(2)	105.1 (17)°	99.833 (3)°	
N(1)–Al(1)–N(2)	2 × 112.6 (15)°	2 × 114.748 (2)°	4 × 112.3 (8)°
		2 × 115.513 (2)°	
N(1)–Al(2)–N(1)		86.801 (1)°	
N(2)–Al(2)–N(2)		94.716 (2)°	
N(1)–Al(2)–N(2)		2 × 119.135 (2)°	
		2 × 119.835 (2)°	

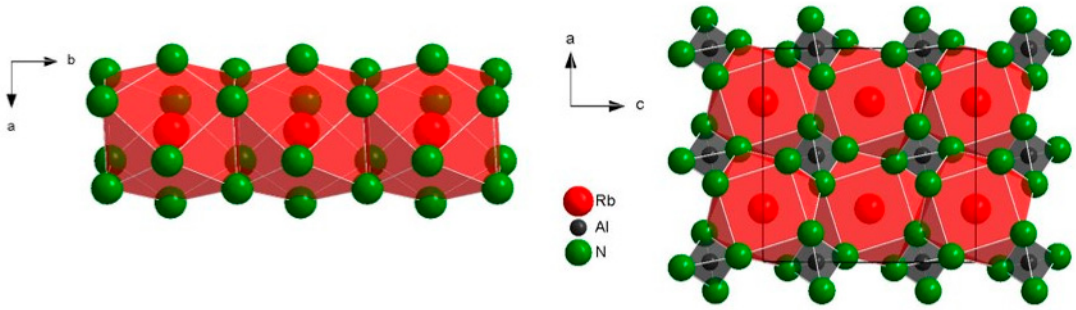

Figure 3. Strands of cuboctahedral-coordinated rubidium in the new monoclinic modification in space group *C*2/*c* extending along the *b*-axis (**left**). Cross-section of the *a*-*b*-plane with polyhedra around Al(1) and Rb (**right**). The structural motif of the cuboctahedra is identical in the tetragonal structure.

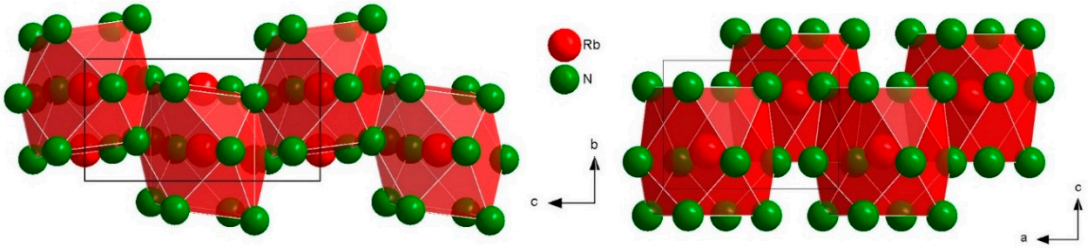

Figure 4. Comparison of the arrangement of cuboctahedra around Rb in $Rb[Al(NH_2)_4]$ in both space group *C*2/*c* (**left**) and *P*4/*n* (**right**).

Both modifications in common, the rubidium and amide ions together form the motif of a distorted cubic close packing—however, with different occupation of the tetrahedral holes only formed by amide ions by aluminum. Locally, this leads to different arrangements of $[Al(NH_2)_4]^-$-tetrahedra in the surrounding of rubidium ions. In order to form the cuboctahedral surrounding, in both forms,

four tetrahedra provide edges and four tetrahedra vertices. While in the tetragonal modification, all vertex-sharing tetrahedra are located on one side of the cuboctahedron, in the monoclinic form, they are more evenly distributed around the central rubidium ion (Figure 5).

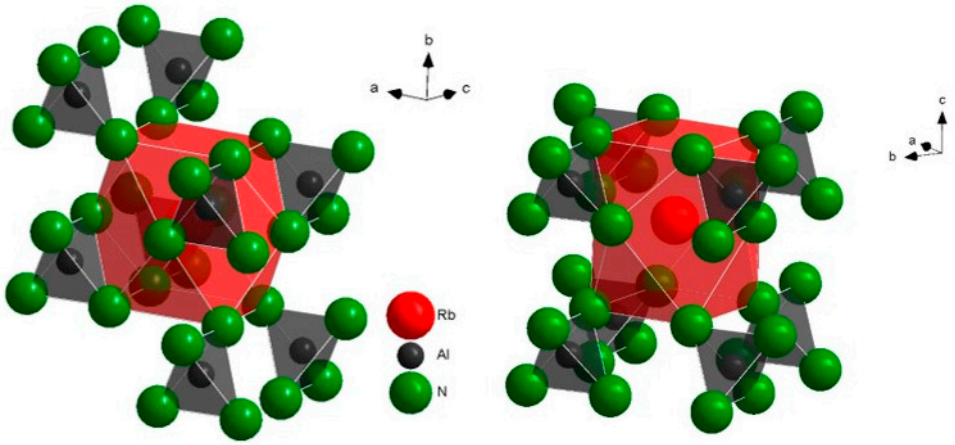

Figure 5. Arrangement of tetraamidogallate-tetrahedra in the surrounding of Rb in the new monoclinic modification in space group *C*2/*c* (**left**) and in the tetragonal structure in *P*4/*n* (**right**).

Within the tetragonal structure, the cuboctahedra around rubidium are connected by face-sharing parallel to the *c*-axis, therefore forming strands. The already mentioned $[Al(NH_2)_4]^-$-tetrahedra are found in layers parallel (110), alternating in edge- and corner-sharing with the cuboctahedra. In the monoclinic modification, in contrast, there are layers composed of two corner-sharing tetrahedra as well as two edge-sharing with the cuboctahedra which extend parallel to the *b*-axis in (101) (Figure 5). The cuboctahedra surrounding rubidium show the same face-sharing as in the *P*4/*n* modification, although parallel to the *b*-axis (compare Figure 3). Furthermore, they are connected via edge-sharing orthogonal to the *b*-axis, similar to the tetragonal structure.

Similar cases of polymorphs of amidometalates differing solely in arrangements of amidometalate tetrahedra and coordination polyhedra of alkali or alkaline earth metal ions turn out to be rather frequent, with recent examples being the three forms of $Ba[Ga(NH_2)_4]_2$ [17] or the low and high temperature phases of $Rb_2[Mn(NH_2)_4]$ [19].

The known tetragonal modification was obtained under similar conditions at 393–443 K and 800–1200 bar, thus at lower temperatures and higher pressures than the new monoclinic form. The slightly smaller volume of V_{tetra} = 147.69 × 10^6 pm^3 compared to V_{mono} = 147.97 × 10^6 pm^3 per formula unit does not give a simple clue about phase relations between both phases, since the exact composition may play a decisive role for the unit cell volume. This is also expressed in the significantly larger volume of the reported powder X-ray diffraction data of an earlier observed monoclinic modification of unknown crystal structure (*P*2/*c*, see Table 1) [18]. Additionally, we have observed single crystals with generally the same symmetry but significantly smaller monoclinic unit cell parameters and thus volume for the new modification in *C*2/*c* (see Table 1). Refinements of the crystal structure resulted in the same monoclinic structure as described above; however, a close inspection revealed additional electron density in further tetrahedral voids formed by amide ions, while the nominal aluminum and nitrogen sites are only occupied to less than unity. Upon occupation of the additional sites with further Al atoms (Figure 6), the reliability factors dropped from *R*1 = 0.1005 and *wR*2 = 0.2805 to 0.0647 and 0.1670, respectively. The observed apparent disorder we interpret in analogy to that observed for the respective liquid amidogallate system [11]: already at ambient temperature, the material loses ammonia, leading to condensation of the tetraamidoaluminate tetrahedra to form edge-sharing binuclear units in solid state according to:

$$2\,[Al(NH_2)_4]^- \rightarrow [(NH_2)_2Al(NH)_2Al(NH_2)_2]^{2-} + 2\,NH_3 \quad (2)$$

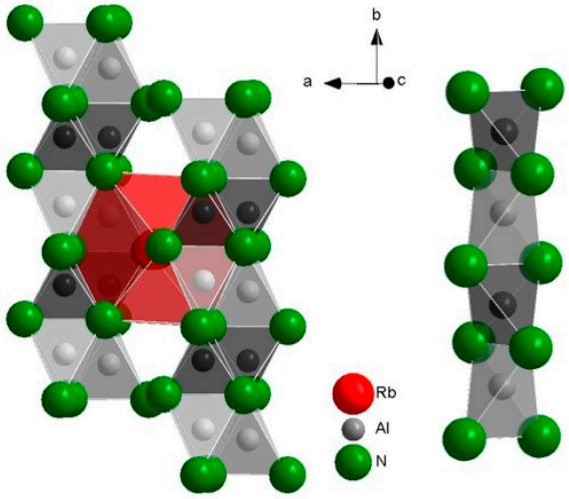

Figure 6. Disordering of $[Al(NH_2)_4]^-$-tetrahedra in the monoclinic modification according to scXRD: Al(1) and Al(2) sites are shown in darker and lighter grey, respectively. The tetrahedra around the two Al sites connect edge-sharing to strands parallel to the *b*-axis.

The slow loss of ammonia over time at even ambient temperature from the material can be observed as a corrosive gas escaping, while the formerly whitish-grey powder seems to get darker, starting to liquefy and become viscous, comparable to honey. Elemental analysis of differently aged samples showed lower nitrogen amounts than expected, averaging at around 90% of the expected percentage (see Table 2). Additionally, the ammonia loss even at ambient temperature can be observed in the results of thermogravimetric measurements as discussed below. These facts can explain the reduced volume and occupation of the nitrogen site, while the two occupied aluminum positions in the structure refinements add up to the expected aluminum content.

Structurally, the nominally empty tetrahedral holes are equivalent to those fully occupied by Al(1) in the ideal structure of the tetraamidoaluminate. When including the disordered aluminum positions, the resulting $[Al(NH_2)_4]^-$-tetrahedra form edge-sharing strands parallel to the *b*-axis. Occupation of a nominally empty tetrahedral void by Al(2) locally leads to formation of a $[(NH_2)_2Al(NH)_2Al(NH_2)_2]^{2-}$ condensed ion, if the neighboring voids within the same strand are empty, explaining the reduced occupation of the Al(1) site. Resulting distances between aluminum atoms within the resulting binuclear amidoimidoaluminate ions of around 252(1) pm (see Table 3) are similar to those observed in nitridoaluminates $Sr_3[Al_2N_6]$ and $Ba_3[Al_2N_6]$, with 254 pm and 256 pm, respectively [25,26]. The latter compounds contain similar edge-sharing units $[N_2AlN_2AlN_2]^{6-}$; thus, the observed deprotonation and condensation in solid state may be interpreted as early steps in nitridoaluminate formation. We have earlier observed analogous behavior of the liquid intermediates in the system $Cs[Ga(NH_2)_4]$-$Cs_2[(NH_2)_2Ga(NH)_2Ga(NH_2)_2]$, which, close to ambient temperature, can variably take up or release amounts of ammonia depending on the applied pressure and temperature conditions [11].

3.1. Thermal Analysis

To further study the decomposition behavior of the amidoaluminate under increased temperature, thermal gravimetric experiments (TG) were conducted on the obtained microcrystalline powder. When using a heating rate of 10 K/min up to 1000 °C, three steps of decomposition are observed (Figure 7). The first two steps occur up to 200 and 350 °C, respectively, with a loss of mass around 8% each. Here, most likely, ammonia is leaving the compound, resulting in condensation products like $Rb_2[Al_2(NH)_2(NH_2)_4]$ first, followed by the formation of AlN and $RbNH_2$. To further investigate these steps, another part of the sample was heated in a glass tube under argon atmosphere so as to visually observe the transitions. When reaching temperatures above 300 °C, liquefying was detected, which continued until around 350 °C, at which, visually, a liquid in the glass aperture could be

observed. Additionally, the color changed, gradually getting darker to brown and later even to a black substance. When heating above 350 °C, the liquid starts to release gas, indicted by small bubbles, and solidifies again, with a concomitant significant decrease in volume. Similar liquefying under the release of ammonia was earlier reported for $Na[Al(NH_2)_4]$ [27]. Intermediates in the ammonobasic GaN synthesis with amides of the heavier alkali metals K–Cs typically are obtained as liquids with variable ammonia content and the tendency to solidify after time [11].

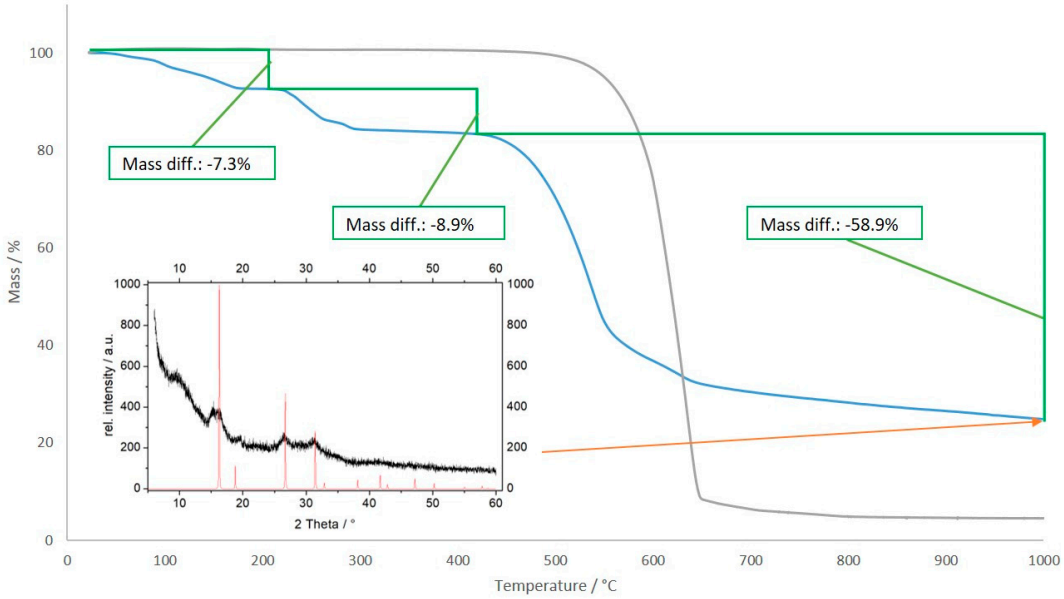

Figure 7. Thermal gravimetric measurement of $Rb[Al(NH_2)_4]$ (blue) and comparison with decomposition/vaporization of $RbNH_2$ (grey). Inset: powder diffraction pattern from the obtained product at 1000 °C together with the simulated pattern for well-crystallized cubic AlN in $F\bar{4}3m$ (red) [24].

The TG curve reveals that the loss of ammonia already slowly starts at or below ambient temperature. Furthermore, loss of one molecule ammonia per formula unit $Rb[Al(NH_2)_4]$ for the first two steps should result in steps of 9.7%, significantly larger than particularly the first step of 7.3% weight loss, also indicating an earlier partial loss of ammonia.

The eventual formation of AlN and $RbNH_2$ after the second step in the TG (thermal gravimetry) is supported by rubidium amide then leaving the mixture at 450 °C onwards, with a mass loss of 58.9%, to leave aluminum nitride in badly crystallized cubic structure in the crucible. For comparison, the decomposition of pure $RbNH_2$ is added to Figure 7. The thermal decomposition seems to result in nano-crystalline AlN, as a powder diffraction of the residue after DTA (differential thermal analysis) shows very broad reflection fitting to cubic sphalerite-type AlN [28]. The stable modification of AlN is hexagonal wurtzite-type; however, sphalerite-type AlN has been reported to form from carbothermal nitridation of Al_2O_3 [29]. Consulting the Scherrer equation, the broadened peaks result in a mean particle size of approximately 2.5 nm.

3.2. Spectroscopy

As expected, the infrared (IR) spectroscopy conducted on the new modification of rubidium tetraamidoaluminate shows little difference to the reported data for the tetragonal modification in *P*4/*n* [18]. This is not surprising considering that the only difference lies in the alignment of the tetrahedra, while the main structure motifs are unchanged but for distortion. The observed signals of IR and Raman spectroscopy have been summarized in Table 4 in comparison to the literature data for the tetragonal modification. Furthermore, a graphic representation of both the measured IR spectrum as well as segments from the Raman spectrum is shown in Figure 8.

Table 4. Measured data of infrared and Raman spectroscopy for both modifications of $Rb[Al(NH_2)_4]$ in space groups *C*2/*c* and *P*4/*n*. The observed signals were assigned to different asymmetric (as) and symmetric (sym) vibrations.

	Infrared/cm^{-1}		Raman/cm^{-1}
	Tetragonal [18]	**Monoclinic**	**Monoclinic**
Valence modes			
$\nu_{as}(NH_2^-)$	3400	3400	3407
	3330	3333	3334
$\nu_{sym}(NH_2^-)$	3255	3250	
	3200	3190	
Deformation modes			
δ_{bend}(HNH)	1563	1544	
	1545		
δ(N-H)		1241	
Al–N lattice modes			
	820	915	
	680	773	
	555	631	586
	523	608	

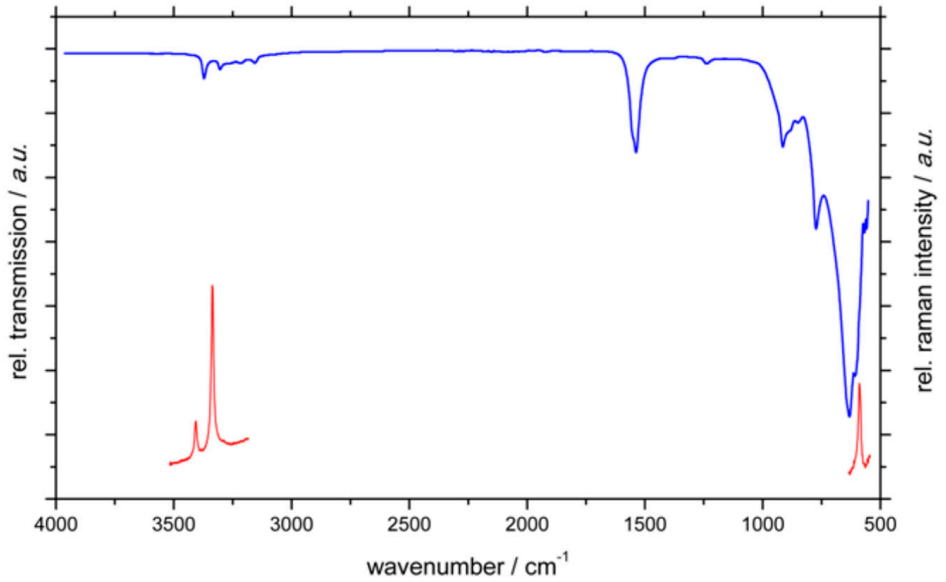

Figure 8. Vibrational spectra of $Rb[Al(NH_2)_4]$ in the monoclinic modification (*C*2/*c*). The infrared spectrum is shown in blue, Raman sections are shown red.

Since the amide ion displays a C_{2v} symmetry, we find several vibration modes, both symmetric and asymmetric, in IR and Raman spectroscopy. For both the symmetric and asymmetric valence vibrations, we find doublets at 3400 and 3250 cm^{-1} alike. In the Raman spectrum, we can still observe the asymmetric valence mode, while the symmetric one does not appear.

At 1544 and 1241 cm^{-1}, we can observe two signals for the bending deformation of the amide ion. When compared to the measurement of the tetragonal structure, we noticed that the second signal is shifted to a lower wave number, although still within range for bending vibrations. At the fingerprint section, the Al–N lattice vibrations can be found. In the Raman spectrum, we could also observe at least one lattice vibration mode, although possible additional signals could not be found due to noise in the spectrum.

4. Conclusions

A new modification of $Rb[Al(NH_2)_4]$ in *C*2/*c* was obtained and the crystal structure determined by powder X-ray diffraction. Thermal analysis indicates decomposition in three steps via a liquid phase with approximate composition $Rb_2[Al_2(NH)_2(NH_2)_4]$ prior to the formation of cubic nano-AlN. However, decomposition and condensation of amidoaluminate ions apparently already starts at ambient temperature within solid state, as indicated by thermal and elemental analysis as well as the results of single crystal X-ray diffraction performed on an aged crystal.

Author Contributions: Conceptualization, C.B. and R.N.; methodology, C.B.; validation, C.B. and R.N.; formal analysis, C.B.; investigation, C.B.; resources, R.N.; data curation, C.B.; writing—original draft preparation, C.B.; writing—review and editing, R.N.; visualization, C.B. and R.N.; supervision, R.N.; project administration, R.N.; funding acquisition, R.N. All authors have read and agreed to the published version of the manuscript.

Funding: This research was funded by the German Research Foundation during the Ammono-FOR 1600 project and within grant NI489/16-1.

Acknowledgments: We thank Kevin Bareiß and Marius Papendick for recording Raman and IR spectra, respectively.

Conflicts of Interest: The authors declare no conflict of interest.

References

1. Lan, Y.; Chen, X.; Cao, Y.; Xu, Y.; Xun, L.; Xu, T.; Liang, J. Low-temperature synthesis and photoluminescence of AlN. *J. Cryst. Growth* **1999**, *207*, 247–250. [CrossRef]
2. Dwilinski, R.; Baranowski, J.; Kaminska, M.; Doradziński, R.; Garczyński, J.; Sierzputowski, L. On GaN Crystallization by Ammonothermal Method. *Acta Phys. Pol. A* **1996**, *90*, 763–766. [CrossRef]
3. Hertrampf, J.; Becker, P.; Widenmeyer, M.; Weidenkaff, A.; Schlücker, E.; Niewa, R.; Schluecker, E. Ammonothermal Crystal Growth of Indium Nitride. *Cryst. Growth Des.* **2018**, *18*, 2365–2369. [CrossRef]
4. Li, Y.-D.; Duan, X.-F.; Qian, Y.-T.; Yang, L.; Ji, M.-R.; Li, C.-W. Solvothermal Co-reduction Route to the Nanocrystalline III−V Semiconductor InAs. *J. Am. Chem. Soc.* **1997**, *119*, 7869–7870. [CrossRef]
5. Nicholas, N.J.; Franks, G.V.; Ducker, W.A. The mechanism for hydrothermal growth of zinc oxide. *CrystEngComm* **2012**, *14*, 1232–1240. [CrossRef]
6. Maruska, H.P.; Tietjen, J.J. The preparation and properties of vapor-deposited single-crystalline GaN. *Appl. Phys. Lett.* **1969**, *15*, 327–329. [CrossRef]
7. Tietjen, J.J.; Amick, J.A. The Preparation and Properties of Vapor-Deposited Epitaxial $GaAs_{1-x}P_x$ Using Arsine and Phosphine. *J. Electrochem. Soc.* **1966**, *113*, 724–728. [CrossRef]
8. Juza, R.; Jacobs, H.; Gerke, H. Ammonothermalsynthese von Metallamiden und Metallnitriden. *Ber. Bunsen-Ges. Phys. Chem.* **1966**, *70*, 1103–1105. [CrossRef]
9. Richter, T.M.M.; Niewa, R. Chemistry of Ammonothermal Synthesis. *Inorganics* **2014**, *2*, 29–78. [CrossRef]
10. Zhang, S.; Alt, N.S.A.; Schlücker, E.; Niewa, R. Novel alkali metal amidogallates as intermediates in ammonothermal GaN crystal growth. *J. Cryst. Growth* **2014**, *403*, 22–28. [CrossRef]
11. Hertrampf, J.; Schlücker, E.; Gudat, D.; Niewa, R. Dissolved Intermediates in Ammonothermal Crystal Growth: Stepwise Condensation of $[Ga(NH_2)_4]^-$ toward GaN. *Cryst. Growth Des.* **2017**, *17*, 4855–4863. [CrossRef]
12. Zhang, S.; Hintze, F.; Schnick, W.; Niewa, R. Intermediates in Ammonothermal GaN Crystal Growth under Ammonoacidic Conditions. *Eur. J. Inorg. Chem.* **2013**, *2013*, 5387–5399. [CrossRef]
13. Wang, B.; Callahan, M.; Rakes, K.; Bouthillette, L.; Wang, S.-Q.; Bliss, D.; Kolis, J. Ammonothermal growth of GaN crystals in alkaline solutions. *J. Cryst. Growth* **2006**, *287*, 376–380. [CrossRef]
14. Wang, B.; Callahan, M.J. Transport growth of GaN crystals by the ammonothermal technique using various nutrients. *J. Cryst. Growth* **2006**, *291*, 455–460. [CrossRef]
15. Ehrentraut, D.; Hoshino, N.; Kagamitani, Y.; Yoshikawa, A.; Fukuda, T.; Itoh, H.; Kawabata, S. Temperature effect of ammonium halogenides as mineralizers on the phase stability of gallium nitride synthesized under acidic ammonothermal conditions. *J. Mater. Chem.* **2007**, *17*, 886–893. [CrossRef]
16. Yoshida, K.; Aoki, K.; Fukuda, T. High-temperature acidic ammonothermal method for GaN crystal growth. *J. Cryst. Growth* **2014**, *393*, 93–97. [CrossRef]

17. Hertrampf, J.; Alt, N.S.A.; Schlücker, E.; Niewa, R. Three Solid Modifications of $Ba[Ga(NH_2)_4]_2$: A Soluble Intermediate in Ammonothermal GaN Crystal Growth. *Eur. J. Inorg. Chem.* **2017**, *2017*, 902–909. [CrossRef]
18. Jacobs, H.; Jänichen, K. Darstellung und Kristallstruktur von Tetraamido-Aluminaten des Rubidiums und Caesiums, $Rb[Al(NH_2)_4]$ und $Cs[Al(NH_2)_4]$. *J. Less Common Met.* **1990**, *159*, 315–325. [CrossRef]
19. Cao, H.; Guo, J.; Chang, F.; Pistidda, C.; Zhou, W.; Zhang, X.; Santoru, A.; Wu, H.; Schell, N.; Niewa, R.; et al. Transition and Alkali Metal Complex Ternary Amides for Ammonia Synthesis and Decomposition. *Chem. A Eur. J.* **2017**, *23*, 9766–9771. [CrossRef]
20. Alt, N.S.; Meissner, E.; Schluecker, E. Development of a novel in situ monitoring technology for ammonothermal reactors. *J. Cryst. Growth* **2012**, *350*, 2–4. [CrossRef]
21. Zhang, S. Intermediates during the Formation of GaN under Ammonothermal Conditions. Ph.D. Thesis, University of Stuttgart, Stuttgart, Germany, 2014.
22. Hüttig, G.F. Apparat zur gleichzeitigen Druck- und Raummessung von Gasen. (Tensi-Eudiometer.). *Z. Anorg. Allg. Chem.* **1920**, *114*, 161–173. [CrossRef]
23. Rodríguez-Carvajal, J. *Introduction to the Program Fullprof: Refinement of Crystal and Magnetic Structures from Powder and Single Crystal Data*; CEA: Saclay, France, 2001.
24. Sheldrick, G.M. Crystal structure refinement with SHELXL. *Acta Crystallogr. Sect. C Struct. Chem.* **2015**, *C71*, 3–8. [CrossRef]
25. Blase, W.; Cordier, G.; Ludwig, M.; Kniep, R. $Sr_3[Al_2N_4]$: A Nitridoaluminate with Corrugated Tetrahedral Chains $^1_\infty[AlN_{4/2}{}^{3-}]$. *Z. Naturforsch. B* **1994**, *49*, 501–505. [CrossRef]
26. Ludwig, M.; Niewa, R.; Kniep, R. Dimers [Al2N6]12- and Chains $^1_\infty[AlN_{4/2}{}^{3-}]$ in the Crystal Structures of $Ca_6[Al_2N_6]$ and $Ba_3[Al_2N_4]$. *Z. Naturforsch. B* **1999**, *54*, 461–465. [CrossRef]
27. Jacobs, H. Neubestimmung von Struktur und Eigenschaften isotyper Natriumtetraamidometallate des Aluminiums und Galliums. *Z. Anorg. Allg. Chem.* **1993**, *619*, 381–386. [CrossRef]
28. Wright, A.F.; Nelson, J.S. Consistent structural properties for AlN, GaN, and InN. *Phys. Rev. B* **1995**, *51*, 7866–7869. [CrossRef]
29. Wang, J.; Wang, W.; Ding, P.; Yang, Y.; Fang, L.; Esteve, J.; Polo, M.; Sánchez, G. Synthesis of cubic aluminum nitride by carbothermal nitridation reaction. *Diam. Relat. Mater.* **1999**, *8*, 1342–1344. [CrossRef]